

Primordial Black Hole Formation via Inverted Bubble Collapse

Kai Murai,^{1,*} Kodai Sakurai,^{1,†} and Fuminobu Takahashi^{1,‡}

¹*Department of Physics, Tohoku University, Sendai, Miyagi 980-8578, Japan*

We propose a novel mechanism of primordial black hole (PBH) formation through inverted bubble collapse. In this scenario, bubbles nucleate sparsely in an incomplete first-order phase transition, followed by a bulk phase transition in the rest of the universe that inverts these pre-existing bubbles into false vacuum regions. These spherically symmetric false-vacuum bubbles subsequently collapse to form PBHs. Unlike conventional PBH formation mechanisms associated with domain wall collapse or bubble coalescence, our inverted bubble collapse mechanism naturally ensures spherical collapse. We demonstrate that, when applied to the electroweak phase transition, this mechanism can produce highly monochromatic PBHs with masses up to $\mathcal{O}(10^{-6} - 10^{-5})M_{\odot}$, which potentially explain the microlensing events observed in the OGLE and Subaru HSC data.

I. INTRODUCTION

The composition of our Universe presents one of the most profound mysteries in modern cosmology. Observational evidence indicates that approximately one-quarter of the energy density of the Universe consists of dark matter, whose nature remains unknown [1–3]. Among various candidates proposed to explain dark matter, primordial black holes (PBHs) stand out as an intriguing possibility [4–8]. While PBHs could potentially account for all of the dark matter, they might also coexist with other dark matter components. Indeed, scenarios in which PBHs constitute a non-negligible fraction or even all of the dark matter have been widely studied. [7, 9–11].

The formation of PBHs requires significant density perturbations in the early Universe. Many proposed mechanisms rely on superhorizon-scale fluctuations, with one widely studied scenario involving the generation of large curvature perturbations during inflation that later reenter the horizon and collapse into PBHs [4–6, 12–15]. However, such scenarios often require fine-tuning of the inflaton potential, particularly in creating ultra-flat regions in the case of single-field inflation models, which imposes non-trivial constraints on inflationary model building. Another possibility is to make use of the large isocurvature perturbations of baryons or dark matter. For instance, PBH formation from collapsing baryon/axion bubbles represents an interesting realization of such a mechanism [16–24].

Alternative mechanisms for generating large overdensities include those involving topological defects such as domain walls [25–35] and first-order phase transitions [36–48]. However, these scenarios face fundamental challenges, as the overdense regions are expected to deviate significantly from spherical symmetry, and it remains unclear how much deviation is allowed for successful PBH formation [49]. Furthermore, even if we restrict ourselves to cases where overdense regions are approximately

spherically symmetric, it is difficult to estimate the probability of forming such nearly spherical overdense regions. These uncertainties make it challenging to predict the PBH abundance and understand the collapse process.

In this Letter, we propose a novel mechanism for PBH formation through inverted bubble collapse in an incomplete first-order phase transition followed by a bulk transition. In our scenario, bubbles sparsely nucleate during an incomplete first-order phase transition. These bubbles are spherically symmetric when nucleated [50], and maintain this symmetry unless they collide. Crucially, before this transition is completed, a second phase transition occurs throughout the Universe except within the bubbles, transforming the bubble interiors into false vacuum regions. Consequently, the initially expanding bubbles begin to contract and eventually collapse. When sufficiently energetic bubbles collapse, they can form PBHs while naturally preserving spherical symmetry. Unlike PBH formation scenarios involving topological defect collapse or bubble coalescence, our mechanism allows for precise prediction of PBH abundance in terms of model parameters due to this preserved spherical symmetry.

While this mechanism itself is a general PBH formation scenario not limited to any specific phase transitions, we demonstrate its realization in the context of the electroweak phase transition (EWPT) by extending the Standard Model (SM) with a singlet scalar field. In this setup, an initial (incomplete) first-order phase transition occurs in the singlet direction, followed by the EWPT in the Higgs direction. We show that this scenario can produce highly monochromatic PBHs with masses up to $\mathcal{O}(10^{-6} - 10^{-5})M_{\odot}$, which could potentially explain the microlensing events observed in the OGLE and Subaru HSC data [51–53] and will also be probed by the ongoing Subaru HSC searches for PBHs and other compact objects. Depending on the model parameters, it can also generate PBHs with much smaller masses that could explain all dark matter. Furthermore, if the EWPT is also of first-order, it could generate gravitational waves detectable by future space-borne interferometers such as LISA [54] (see also Refs. [55–63] for the studies of theoretical predictions of gravitational waves in the extension of the SM with a real singlet scalar.) Indeed, as we will

* kai.murai.e2@tohoku.ac.jp

† kodai.sakurai.e3@tohoku.ac.jp

‡ fumi@tohoku.ac.jp

see, for the model parameters we adopt, the phase transition in the Higgs direction is of first order.

II. PBH FORMATION IN THE INVERTED BUBBLE COLLAPSE

In this section, we derive the mass distribution of PBHs formed through our inverted bubble collapse mechanism. We first calculate the bubble size distribution, then determine their collapse conditions and derive the mass spectrum of PBHs.

To calculate the bubble size distribution, we first need to track the evolution of bubbles in the cooling universe. We evaluate this at time $t = t_c$, when the bubble walls start to shrink after their interiors have become false vacuum regions through the bulk phase transition. Note that t_c is generically later than the bulk phase transition that occurs at $t = t_{PT}$. The bubble nucleation rate per unit volume, $\Gamma(T)$, depends on the cosmic temperature T and grows exponentially as the universe cools down.

Well before the bubble percolation, the number density of the bubbles, $n_b(t)$, satisfies

$$\frac{dn_b}{dt} = -3Hn_b + \Gamma(T(t)). \quad (1)$$

The solution to this equation is

$$n_b(t)a^3(t) = e^{\int^t dt' a^3(t')\Gamma(T(t'))}. \quad (2)$$

With this solution for the bubble number density, we can derive the size distribution. A key ingredient is the relation between a bubble's nucleation time t_n and its size R at $t = t_c$. Assuming that each bubble expands with a constant velocity v after nucleation, the size at $t = t_c$ is given by

$$\begin{aligned} R(t_c; t_n) &= a(t_c) \left(\frac{R_{\text{in}}}{a(t_n)} + \int_{t_n}^{t_c} d\tilde{t} \frac{v}{a(\tilde{t})} \right) \\ &= \sqrt{\frac{t_c}{t_n}} R_{\text{in}} + 2vt_c \left[1 - \left(\frac{t_n}{t_c} \right)^{1/2} \right], \end{aligned} \quad (3)$$

where a is the scale factor, and R_{in} is the physical critical radius at the bubble nucleation. In the second equality, we used $a \propto t^{1/2}$, as we focus on PBH formation during the radiation-dominated (RD) era in this Letter. As a result, the size distribution of the bubble at $t = t_c$ is given by

$$\begin{aligned} \frac{dn_b}{dR}(t_c) &= \left| \frac{dt_R}{dR(t_c; t_R)} \right| \frac{1}{a(t_c)^3} \frac{dn_b a^3}{dt}(t_R) \\ &= \frac{\Gamma(T_R) t_R^2}{v t_c^2} \left(1 + \frac{R_{\text{in}}}{2vt_R} \right)^{-1}, \end{aligned} \quad (4)$$

where t_R is the nucleation time of a bubble whose radius is R at $t = t_c$, i.e., t_R is the time satisfying $R(t_c; t_R) = R$, and we define $T_R \equiv T(t_R)$. Typically, the contribution of

R_{in} in Eq. (3) becomes negligibly small soon after bubble nucleation, so it can be dropped. Then, we obtain

$$t_R \simeq t_c \left(1 - \frac{R}{2vt_c} \right)^2, \quad (5)$$

and

$$\begin{aligned} \frac{dn_b}{dR}(t_c) &\simeq \frac{\Gamma(T(t_R)) t_R^2}{v t_c^2} \\ &\simeq \frac{\Gamma(T(t_R))}{v} \left(1 - \frac{R}{2vt_c} \right)^4. \end{aligned} \quad (6)$$

Note that the bubble radius is bounded by the sound horizon as

$$R \lesssim 2vt_c. \quad (7)$$

Next, we discuss the PBH formation from a false bubble. Here, we denote the potential energy difference between the inside and outside of the bubble by ΔV , which we treat as constant during the relevant timescale of bubble collapse. In realistic situations, ΔV depends on temperature, as we will see later; however, for simplicity, we treat it as a constant in the following analysis.

Let us assume that the radius of the bubble is R when its interior transitions to the false vacuum and the bubble wall starts to shrink. Then, the energy of the bubble can be approximately expressed as

$$M_b \simeq \frac{4\pi}{3} R^3 \Delta V. \quad (8)$$

As the bubble shrinks, a part of the vacuum energy swept by the bubble wall is accumulated in the kinetic energy of the wall, and this energy gets progressively concentrated inside a smaller region. When the first-order phase transition is sufficiently strong with a large vacuum energy difference, the bubble wall can undergo run-away acceleration despite the dissipation through interactions with the ambient plasma [64]. In such run-away cases, we introduce an efficiency parameter $\epsilon (\leq 1)$ to characterize the fraction of vacuum energy converted into the wall's kinetic energy. Then, if the bubble size becomes smaller than the Schwarzschild radius, $R_s = 2G\epsilon M_b$, the bubble collapses into a PBH. Considering that the bubble can be as small as the width of the bubble wall, δ , the condition for the PBH formation is given by¹

$$R_s = 2G\epsilon M_b \simeq \frac{\epsilon R^3 \Delta V}{3M_{\text{Pl}}^2} \gtrsim \delta. \quad (9)$$

Considering the upper bound of the bubble radius, we obtain the allowed range of the PBH mass as

$$M_{\text{min}} \equiv \frac{\delta}{2G} \lesssim M \lesssim M_{\text{max}} \equiv \frac{32\pi}{3} \epsilon v^3 t_c^3 \Delta V. \quad (10)$$

¹ In fact, the bubble wall width becomes thinner due to the Lorentz contraction as it gets accelerated. The wall width δ is assumed to include this effect.

Since the bubble size never exceeds the particle horizon, the false vacuum energy inside the bubble does not dominate the universe before collapsing into a PBH. Thus, $\Delta V \lesssim 3M_{\text{Pl}}^2 H^2$ holds until the PBH is formed. As a result, we obtain the condition for ΔV given by

$$\frac{3M_{\text{Pl}}^2 \delta}{\epsilon R^3} \lesssim \Delta V \lesssim 3M_{\text{Pl}}^2 H_c^2 = \frac{\pi^2 g_* T_c^4}{30}, \quad (11)$$

where H_c and T_c denote the Hubble parameter and temperature when $t = t_c$, respectively. In the following, we assume that M_{min} is much smaller than the mass region of interest, which is a condition typically satisfied in realistic situations.²

Taking into account the size distribution of the bubbles, we obtain the mass function of the PBHs given by

$$\begin{aligned} \frac{d\rho_{\text{PBH}}}{d \ln M}(t) &= M \frac{dn_b}{dR}(t_c) \frac{dR}{d \ln M_b} \left(\frac{a(t_c)}{a(t)} \right)^3 \Theta(M - M_{\text{min}}) \\ &= \frac{MR \Gamma(T_R)}{3} \frac{t_R^2}{v} \left(\frac{a(t_c)}{a(t)} \right)^3 \Theta(M - M_{\text{min}}), \end{aligned} \quad (12)$$

where R is related to M_b via Eq. (8), $M = \epsilon M_b$, and t represents the time after the PBH formation.

Next, we evaluate the PBH mass function assuming the temperature dependence of the bubble nucleation rate. The bubble nucleation rate is considered to increase progressively toward the bulk phase transition that occurs at temperature $T = T_{\text{PT}} (\geq T_c)$, and then effectively drops down to zero afterwards. Thus, around the bulk phase transition, it can be parametrized as³

$$\Gamma(T) \simeq \begin{cases} c H_{\text{PT}}^4 e^{-\alpha \frac{T - T_{\text{PT}}}{T_{\text{PT}}}} & \text{for } T \geq T_{\text{PT}} \\ 0 & \text{for } T \leq T_{\text{PT}} \end{cases}, \quad (13)$$

where H_{PT} is the Hubble parameter at the bulk phase transition, and c and α are constant parameters. From Eqs. (5) and (8), we obtain

$$\begin{aligned} T_R &= \sqrt{\frac{t_c}{t_R}} T_c \\ &\simeq \left(1 - \frac{R}{2vt_c} \right)^{-1} T_c \\ &\simeq \left[1 - \frac{H_c}{v} \left(\frac{3M}{4\pi\epsilon\Delta V} \right)^{1/3} \right]^{-1} T_c. \end{aligned} \quad (14)$$

² The width of the bubble wall in the rest frame is typically estimated by the inverse of the mass scale of the field driving the phase transition. For instance, if we take the mass scale to be 100 GeV, we obtain $M_{\text{min}} \simeq 6 \times 10^{-22} M_{\odot} / \gamma$ with γ being the Lorentz factor of the wall.

³ We require that the first-order phase transition via bubble nucleation should not occur inside the bubbles, as it would spoil the spherical symmetry and reduce the energy inside them. This condition is met in the case of the singlet extension of the SM studied in the next section.

Then, the mass function is given by

$$\begin{aligned} \frac{d\rho_{\text{PBH}}}{d \ln M}(t) &\simeq \frac{c M H_{\text{PT}}^4}{3v} \left(\frac{3M}{4\pi\epsilon\Delta V} \right)^{1/3} \left[1 - \frac{H_c}{v} \left(\frac{3M}{4\pi\epsilon\Delta V} \right)^{1/3} \right]^4 \left(\frac{a(t_c)}{a(t)} \right)^3 \\ &\quad \times \exp \left[-\alpha \left(\frac{T_c}{T_{\text{PT}}} \left[1 - \frac{H_c}{v} \left(\frac{3M}{4\pi\epsilon\Delta V} \right)^{1/3} \right]^{-1} - 1 \right) \right], \end{aligned} \quad (15)$$

for M satisfying $M_{\text{min}} < M < M_{\text{max}}$ and $T_R > T_{\text{PT}}$. This mass function is translated to the energy ratio to dark matter by

$$\begin{aligned} \frac{df_{\text{PBH}}}{d \ln M} &= \frac{1}{\rho_{\text{DM}}(t)} \frac{d\rho_{\text{PBH}}}{d \ln M}(t) \\ &\simeq \frac{1}{0.44 \text{ eV}} \frac{45}{2\pi^2 g_{*s}(T_c) T_c^3} \frac{c M H_{\text{PT}}^4}{3v} \left(\frac{3M}{4\pi\epsilon\Delta V} \right)^{1/3} \\ &\quad \times \left[1 - \frac{H_c}{v} \left(\frac{3M}{4\pi\epsilon\Delta V} \right)^{1/3} \right]^4 \\ &\quad \times \exp \left[-\alpha \left(\frac{T_c}{T_{\text{PT}}} \left[1 - \frac{H_c}{v} \left(\frac{3M}{4\pi\epsilon\Delta V} \right)^{1/3} \right]^{-1} - 1 \right) \right] \end{aligned} \quad (16)$$

In Fig. 1, we show the predicted PBH abundance in this model. We use the parameter sets (a) and (b) shown in Tab. I for the red and blue solid lines, respectively. These parameter sets correspond to a constant bubble nucleation rate ($\alpha = 0$), fast bubble expansion ($v = 1$), and efficient accumulation of the false vacuum energy ($\epsilon = 1$). For comparison, we also show the results for the cases with $\alpha = 10$ (red dashed line) and with $v = 0.5$ (red dot-dashed line) based on the parameter set (a). Note that v , ϵ , and ΔV appear in Eq. (16) in the form of $v(\epsilon\Delta V)^{1/3}$, and the changes of their values are degenerate in $df_{\text{PBH}}/d \ln M$. In these cases, the mass distribution follows $df_{\text{PBH}}/d \ln M \propto M^{4/3}$ for $M \ll M_{\text{max}}$ and has a cutoff at $M = M_{\text{max}}$. On the other hand, the PBH mass function for the parameter set (b) has a cutoff on smaller mass. This is because all bubbles expand at least between t_{PT} and t_c , and there is a minimal bubble radius at $t = t_c$, leading to the lower bound on the PBH mass. As we will see below, the PBH mass distribution approaches a monochromatic distribution as t_c is significantly delayed from t_{PT} . If we set T_{PT} equal to T_c in the parameter set (b) and tune c , we obtain the same mass function, except that there is no cutoff for small masses as shown in the blue dashed line.

III. MODEL

In this section, we apply the inverted bubble collapse mechanism to the EWPT by introducing a real singlet

TABLE I. Parameter sets for the red and blue solid lines in Fig. 1.

Set	$T_{\text{PT}} [\text{GeV}]$	$T_c [\text{GeV}]$	$\Delta V/\rho_{\text{tot}}(T_c)$	v	ϵ	c	α
(a)	10	10	0.1	1	1	3.0×10^{-9}	0
(b)	3.0×10^4	2.8×10^4	0.1	1	1	1.7×10^{-11}	0

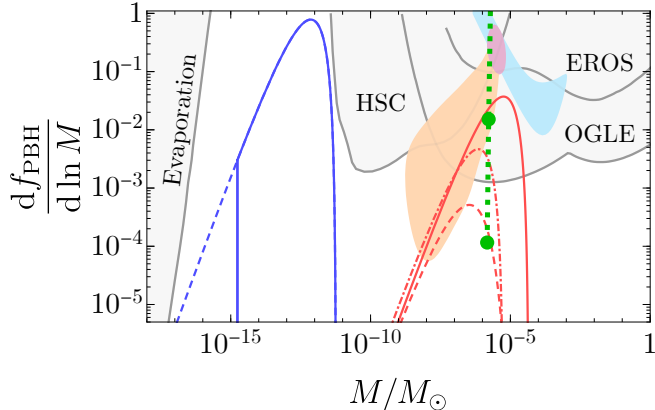


FIG. 1. PBH fraction in dark matter, $df_{\text{PBH}}/d \ln M$. The red and blue solid lines correspond to the parameter sets (a) and (b) in Table. I, respectively. The red dashed and red dotted lines adopt $\alpha = 10$ and $v = 0.5$ based on parameter set (a), respectively. For the blue dashed line, we set T_{PT} equal to T_c in the parameter set (b) and tune c so that it overlaps with the blue solid line for larger masses. The green dots represent the PBH fraction f_{PBH} in the singlet-extended model, with the dotted line showing its variation with the singlet triple coupling. The orange and light blue regions are obtained assuming the lensing event observed in the HSC M31 observation [52] and OGLE [51, 53] are due to PBHs, respectively. The purple region is the joint posterior for them [65]. The gray lines represent the observational upper bounds on the PBH abundance by EROS [66], HSC [52], OGLE-III+OGLE-IV [67], OGLE-IV high cadence survey [68]. The evaporation constraint is taken from PBH bounds [11, 69]

scalar S to the SM Higgs sector. The most general renormalizable scalar potential is given by

$$V(\Phi, S) = -m_\Phi^2 |\Phi|^2 + \lambda |\Phi|^4 + \mu_{\Phi S} |\Phi|^2 S + \lambda_{\Phi S} |\Phi|^2 S^2 + t_S S - m_S^2 S^2 + \mu_S S^3 + \lambda_S S^4, \quad (17)$$

where Φ denotes the Higgs doublet.

We choose the parameters in the scalar potential such that the phase transition proceeds in two stages. Initially, due to a local minimum along the S direction, the S field undergoes a first-order phase transition with bubble nucleation, where the S field takes a larger value inside the bubbles than outside. Subsequently, the Higgs field in the bulk (outside the bubbles) undergoes EWPT at time $t = t_{\text{PT}}$, before the completion of the first-order phase transition in the S direction. While the vacuum state with a non-zero Higgs vacuum expectation value (VEV) in the bulk is not necessarily the true vacuum at t_{PT} , it

evolves into the true vacuum by $t = t_c$. At this point, the bubble interior, where the Higgs field remains in its symmetric phase, becomes a false vacuum, triggering the bubbles to collapse and form PBHs within a few Hubble times.

When t_c is significantly delayed beyond t_{PT} , the resultant PBH mass tends to be larger for two reasons: the continued bubble expansion increases the false vacuum energy inside, and the collapse exhibits more runaway behavior, leading to a larger efficiency parameter ϵ . Additionally, as t_c is delayed, the physical size of bubbles asymptotically approaches the sound horizon size at $t = t_c$. This behavior occurs because no new bubbles form after t_{PT} , and existing bubbles gradually approach the sound horizon. As a consequence, these similarly-sized bubbles collapse to form PBHs with highly monochromatic mass distribution, resulting in a sharp mass peak.

The PBH abundance shown in Fig. 1 corresponds to the parameter choice $v = 246.2 \text{ GeV}$, $m_h = 125.09 \text{ GeV}$, $m_H = 280 \text{ GeV}$, $\theta = 0$, $\lambda_S = 0.586$, $\lambda_{\Phi S} = 0.5$, $\mu_S = [-246.025, -246.1] \text{ GeV}$, $t_S = 0$, $\mu_{\Phi S} = 0$, where v is the EW VEV, m_h (m_H) is the mass of SM-like (heavy) Higgs boson, and θ is the mixing angle for the CP-even Higgs bosons. Due to the extremely narrow mass spectrum in this model, we represent the PBH fraction f_{PBH} by green dots in the figure (using the same numerical scale as $df_{\text{PBH}}/d \ln M$ indicated on the vertical axis), with its variation with the singlet triple coupling shown by the dotted lines (see Appendix A for the detailed spectrum). We have used CosmoTransitions [70] to evaluate the tunneling rate and ΔV in the singlet extension model. For instance, we obtain $T_{\text{PT}} \approx 148 \text{ GeV}$ and $T_c \approx 36 \text{ GeV}$ for the lower green dot in Fig. 1. The existence of such viable parameters in this minimal setup suggests that our PBH formation mechanism can be naturally realized in a wide class of models with multi-step phase transitions. Further details of the model are provided in Appendix A.

IV. DISCUSSION AND CONCLUSIONS

In this Letter, we have proposed a novel PBH formation mechanism through inverted bubble collapse, where sparsely nucleated bubbles in an incomplete first-order phase transition become false vacuum regions after a bulk phase transition. These false vacuum bubbles collapse to form PBHs, allowing for precise prediction of PBH abundance through model parameters owing to the preserved spherical symmetry.

In our inverted bubble collapse mechanism, PBH abundance depends on both the rate and timing of bubble nucleation before the bulk phase transition, making it sensitive to the scalar potential shape. The scalar potential parameters must be set appropriately; the first-order phase transition should remain incomplete, as bubble collisions would break spherical symmetry and complicate PBH formation. If PBHs constitute a significant fraction of dark matter, this parameter constraint may be explained by anthropic selection; a completed first-order transition would trap our universe in a false vacuum, triggering old inflation and diluting baryons, while without a first-order transition, no PBH dark matter would form.

The final PBH mass depends on the detailed properties of the phase transitions. When applied to the EWPT, the PBH mass can reach up to $\mathcal{O}(10^{-6} - 10^{-5})M_\odot$, corresponding to the horizon mass around the EW scale. Note that, as in the case studied in the previous section, it could take some time for the interior of the bubbles to become the false vacuum, which tends to increase the final PBH masses that exhibit a sharp mass distribution peak. This mass range of $\mathcal{O}(10^{-6} - 10^{-5})M_\odot$ is particularly interesting as it could potentially explain the microlensing events observed in the OGLE and Subaru HSC data [51–53], and it will also be probed by future observations.

Smaller PBH masses are also possible, and PBHs generated by this mechanism could account for all dark matter. We have demonstrated that the inverted bubble collapse mechanism can be easily implemented in the EWPT with a real singlet scalar. A comprehensive exploration of the full parameter space remains an interesting direction for future work.

The PBH abundance depends on the properties of the bulk phase transition, with masses generally increasing if the transition is of first order. Interestingly, the first-order phase transition in the bulk will generate gravitational waves that could be probed by the future LISA experiment [54]. Further investigation of baryogenesis scenarios [71, 72] within the inverted bubble collapse framework is left for future investigation.

ACKNOWLEDGMENTS

We thank Katsuya Hashino for useful discussions. This work is supported by JSPS Core-to-Core Program (grant number: JPJSCCA20200002) (F.T.), JSPS KAKENHI Grant Numbers 20H01894 (F.T.), 20H05851 (F.T.), 23KJ0088 (K.M.), 24K17039 (K.M.), and 23KJ0086 (K.S.). This article is based upon work from COST Action COSMIC WISPerS CA21106, supported by COST (European Cooperation in Science and Technology).

Appendix A: Singlet Extension Model for EWPT

In this Appendix, we give a more detailed explanation of the singlet extension model given by Eq. (17). The component fields of Φ and S are given by

$$\Phi = \begin{bmatrix} G^+ \\ \frac{1}{\sqrt{2}}(v + \phi + iG^0) \end{bmatrix}, \quad S = v_S + s, \quad (\text{A1})$$

where $v \simeq 246$ GeV and v_S are the VEVs of Φ and S , respectively, and G^+ and G^0 are Nambu-Goldstone bosons that are absorbed by the weak gauge bosons. The shift of S , $S \rightarrow S + v'_S$, does not change physics [73]. Due to this shift invariance, we take $v_S = 0$ in the following discussion. The CP-even scalar states ϕ and s mix with each other. The mass matrix in the weak basis (s, ϕ) is given by

$$M^2 = \begin{pmatrix} M_{ss}^2 & M_{sh}^2 \\ M_{sh}^2 & M_{hh}^2 \end{pmatrix}, \quad (\text{A2})$$

$$M_{ss}^2 = 2m_S^2 + \lambda_{\Phi S} v^2, M_{sh}^2 = \mu_{\Phi S} v, M_{hh}^2 = 2\lambda v^2. \quad (\text{A3})$$

This mass matrix is diagonalized by the following orthogonal transformation:

$$\begin{pmatrix} s \\ \phi \end{pmatrix} = \begin{pmatrix} \cos\theta & -\sin\theta \\ \sin\theta & \cos\theta \end{pmatrix} \begin{pmatrix} H \\ h \end{pmatrix}. \quad (\text{A4})$$

The mass eigenstates H and h are identified with the heavy Higgs boson and 125 GeV Higgs boson, respectively. With the transformation (A4), the masses of H and h and the mixing angle θ are calculated as

$$m_H^2 = \cos^2\theta M_{ss}^2 + \sin^2\theta M_{hh}^2 + \sin(2\theta)M_{sh}^2, \quad (\text{A5})$$

$$m_h^2 = \sin^2\theta M_{ss}^2 + \cos^2\theta M_{hh}^2 - \sin(2\theta)M_{sh}^2, \quad (\text{A6})$$

$$\tan(2\theta) = \frac{2\mu_{\Phi S} v}{2m_S^2 - v^2(2\lambda - \lambda_{\Phi S})}. \quad (\text{A7})$$

Though these relations and the tadpole conditions of the scalar potential (17), the potential parameters $t_S, m_\Phi^2, \lambda, m_S^2$, and $\mu_{\Phi S}$ can be expressed in terms of the physical masses and mixing parameters as

$$t_S = -\frac{v^2}{2}\mu_{\Phi S}, \quad (\text{A8})$$

$$m_S^2 = \frac{1}{2}(-\sin^2\theta m_h^2 - \cos^2\theta m_H^2 + \lambda_{\Phi S} v^2), \quad (\text{A9})$$

$$m_\Phi^2 = v^2\lambda, \quad (\text{A10})$$

$$\lambda = \frac{1}{2v^2}(\cos^2\theta m_h^2 + \sin^2\theta m_H^2), \quad (\text{A11})$$

$$\mu_{\Phi S} = \frac{1}{v}(m_H^2 - m_h^2)\cos\theta\sin\theta. \quad (\text{A12})$$

We choose the following seven parameters as model input parameters:

$$v, \quad m_h, \quad m_H, \quad \theta, \quad \mu_S, \quad \lambda_S, \quad \lambda_{\Phi S}, \quad (\text{A13})$$

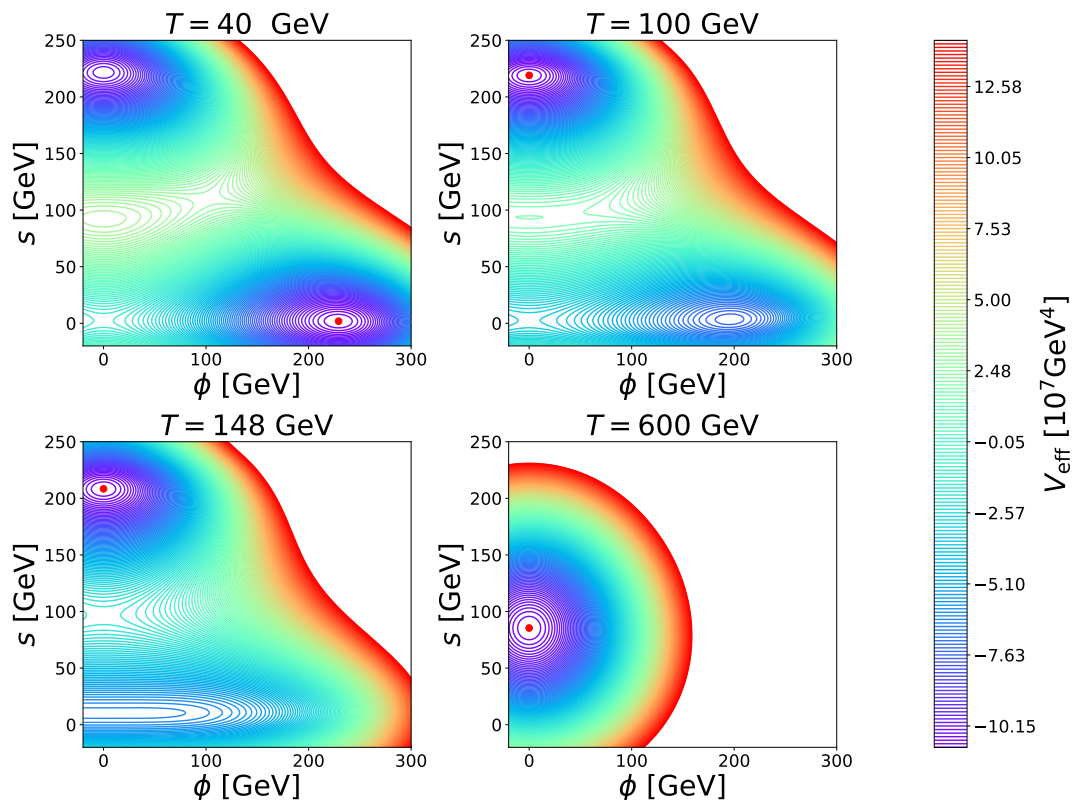


FIG. 2. Contours of the effective potential in the (ϕ, s) plane at temperatures $T = 40, 100, 148,$ and 600 GeV. The red points indicate the global minimum at each temperature.

where the EW VEV and the SM-like Higgs boson mass are fixed to be $v = 246.2$ GeV, $m_h = 125.09$ GeV.

From the potential (17), one can calculate the effective potential, which consists of the three contributions, i.e., $V_{\text{eff}}(\phi, s, T) = V_0(\phi, s) + V_{\text{CW}}(\phi, s) + V_T(\phi, s, T)$, where $V_0(\phi, s)$ is the tree-level potential, $V_{\text{CW}}(\phi, s)$ is Coleman-Weinberg potential up to the one-loop level [74], and $V_T(\phi, s, T)$ is the finite-temperature effect of the effective potential [75]. The tree-level contribution V_0 can be straightforwardly obtained from the potential (17) with the replacement of $(\Phi, S) \rightarrow (\phi, s)$. The remaining parts V_{CW} and V_T depend on the field-dependent masses $m_i^2(\phi, s)$ of the model, for which the concrete expressions are given in, e.g., Refs. [55, 62, 76]. Renormalization of the Coleman-Weinberg potential is performed in the $\overline{\text{MS}}$ scheme, by which the renormalization scale μ_R is introduced in the effective potential.⁴ In our analysis, we set $\mu_R = m_t$. We implement the thermal effects of the field-dependent masses by the replacement $m_i^2(\phi, s) \rightarrow M_i^2(\phi, s, T) = m_i^2(\phi, s) + \Pi_i(T)$ in the effective potential V_{eff} [79], where the temperature-dependent

self-energy $\Pi_i(T)$ is presented in, e.g., Refs. [55, 62, 76].

For the parameter points presented in the main text, we have checked that this parameter point satisfies the theoretical constraints for the scalar potential, i.e., perturbative unitarity [80] and the stability condition of the potential [81]. We have also checked that the EW vacuum is the global minimum at zero temperature with the effective potential, $V_{\text{eff}}(\text{EW vacuum}) < V_{\text{eff}}(S\text{-vacuum})$ at $T = 0$ [82]. Experimental constraints such as direct searches of H and Higgs coupling measurements for the singlet model are discussed with the Run II data of LHC in the Appendix of Ref. [63]. The above parameter point satisfies all these experimental constraints.

For the model parameters adopted in the main text, there are three relevant local minima that appear at different temperatures. At sufficiently high temperatures, there is only a unique vacuum where the EW symmetry is restored. Note that the singlet S has a nonzero VEV in this vacuum, since we do not impose Z_2 symmetry on S . Then as the temperature decreases, another local minimum appears along the S direction. Let us call this minimum the S -vacuum. We have verified that the bubble nucleation rate progressively increases as the universe cools down, where we have used *CosmoTransitions* [70] to evaluate the tunneling rate. This rate becomes insensitive to the cosmic temperature around the EWPT since the S -vacuum exists even when thermal effects are negli-

⁴ The Coleman-Weinberg potential can also be evaluated by applying another renormalization scheme, such as on shell-like schemes. The renormalization scheme difference of the effective potential is discussed in Refs. [77, 78].

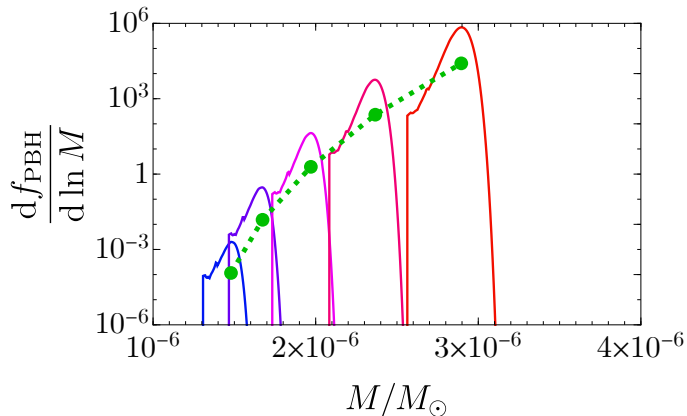


FIG. 3. The highly monochromatic PBH mass spectrum in the singlet-extension model. The spectra from left to right are calculated with different values of the singlet triple coupling $\mu_S = -246.025, -246.1, -246.175, -246.25, -246.325$ GeV, while other parameters are fixed as in the main text. Note that the PBH fraction shown by the green dots is about two orders of magnitude smaller than the peak height due to the extremely narrow width.

gible. Subsequently, the EWPT occurs in the bulk along the Higgs direction. Let us call this vacuum the EW vacuum. For the adopted model parameters, the EWPT is of first order, and completes around $T_{PT} \approx 148$ GeV. The energy difference between the S -vacuum and the EW vac-

uum, ΔV , depends on the cosmic temperature. For the adopted parameters, the EW vacuum is still meta-stable soon after the EWPT, and it becomes the true vacuum around $T_t \approx 40-50$ GeV. To illustrate such phase transitions, Fig. 2 shows the effective potential in the (ϕ, s) plane at different temperatures $T = 40, 100, 148,$ and 600 GeV. We set $\mu_S = -246.025$ GeV, and other input parameters are taken as presented in the main text. One can see that the S -vacuum first appears in the singlet direction, followed by the appearance of the EW vacuum in the Higgs direction.

Fig. 3 shows the highly monochromatic PBH mass spectrum predicted in the singlet-extension model. It should be noted that due to the extremely narrow peak width, the PBH fraction in dark matter obtained by integrating the distribution (green dots) is about two orders of magnitude smaller than the peak height of the mass distribution. This spectrum is obtained by substituting the temperature-dependent bubble nucleation rate and ΔV calculated using CosmoTransition into Eq. (16). We have assumed that the bubbles start to shrink one Hubble time after the EW vacuum becomes the true vacuum and used $T_c = T_t/\sqrt{2}$. Here, the spectra from left to right correspond to different values of the singlet triple coupling $\mu_S = -246.025, -246.1, -246.175, -246.25, -246.325$ GeV, while keeping other parameters fixed as in the main text.

-
- [1] N. Aghanim *et al.* (Planck), *Astron. Astrophys.* **641**, A6 (2020), [Erratum: *Astron. Astrophys.* 652, C4 (2021)], [arXiv:1807.06209 \[astro-ph.CO\]](#).
- [2] V. C. Rubin and W. K. Ford, Jr., *Astrophys. J.* **159**, 379 (1970).
- [3] F. Zwicky, *Helv. Phys. Acta* **6**, 110 (1933).
- [4] S. W. Hawking, *Commun. Math. Phys.* **25**, 152 (1972).
- [5] B. J. Carr and S. W. Hawking, *Mon. Not. Roy. Astron. Soc.* **168**, 399 (1974).
- [6] B. J. Carr, *Astrophys. J.* **201**, 1 (1975).
- [7] P. H. Frampton, M. Kawasaki, F. Takahashi, and T. T. Yanagida, *JCAP* **04**, 023 (2010), [arXiv:1001.2308 \[hep-ph\]](#).
- [8] B. Carr, F. Kuhnel, and M. Sandstad, *Phys. Rev. D* **94**, 083504 (2016), [arXiv:1607.06077 \[astro-ph.CO\]](#).
- [9] B. Carr, K. Kohri, Y. Sendouda, and J. Yokoyama, *Rept. Prog. Phys.* **84**, 116902 (2021), [arXiv:2002.12778 \[astro-ph.CO\]](#).
- [10] B. Carr and F. Kuhnel, *Ann. Rev. Nucl. Part. Sci.* **70**, 355 (2020), [arXiv:2006.02838 \[astro-ph.CO\]](#).
- [11] A. M. Green and B. J. Kavanagh, *J. Phys. G* **48**, 043001 (2021), [arXiv:2007.10722 \[astro-ph.CO\]](#).
- [12] Y. B. Zel'dovich and I. D. Novikov, *Sov. Astron.* **10**, 602 (1967).
- [13] J. Yokoyama, *Astron. Astrophys.* **318**, 673 (1997), [arXiv:astro-ph/9509027](#).
- [14] J. García-Bellido, A. Linde, and D. Wands, *Phys. Rev. D* **54**, 6040 (1996), [arXiv:astro-ph/9605094 \[astro-ph\]](#).
- [15] M. Kawasaki, N. Sugiyama, and T. Yanagida, *Phys. Rev. D* **57**, 6050 (1998), [arXiv:hep-ph/9710259 \[hep-ph\]](#).
- [16] A. Dolgov and J. Silk, *Phys. Rev. D* **47**, 4244 (1993).
- [17] A. D. Dolgov, M. Kawasaki, and N. Kevlishvili, *Nucl. Phys. B* **807**, 229 (2009), [arXiv:0806.2986 \[hep-ph\]](#).
- [18] M. Kawasaki and K. Murai, *Phys. Rev. D* **100**, 103521 (2019), [arXiv:1907.02273 \[astro-ph.CO\]](#).
- [19] N. Kitajima and F. Takahashi, *JCAP* **11**, 060 (2020), [arXiv:2006.13137 \[hep-ph\]](#).
- [20] M. Kawasaki, K. Murai, and H. Nakatsuka, *JCAP* **10**, 025 (2021), [arXiv:2107.03580 \[astro-ph.CO\]](#).
- [21] K. Kasai, M. Kawasaki, and K. Murai, *JCAP* **10**, 048 (2022), [arXiv:2205.10148 \[astro-ph.CO\]](#).
- [22] K. Kasai, M. Kawasaki, N. Kitajima, K. Murai, S. Neda, and F. Takahashi, *JCAP* **10**, 049 (2023), [arXiv:2305.13023 \[astro-ph.CO\]](#).
- [23] K. Kasai, M. Kawasaki, N. Kitajima, K. Murai, S. Neda, and F. Takahashi, *JCAP* **05**, 092 (2024), [arXiv:2310.13333 \[astro-ph.CO\]](#).
- [24] K. Kasai, M. Kawasaki, K. Murai, and S. Neda, (2024), [arXiv:2405.09790 \[astro-ph.CO\]](#).
- [25] F. Ferrer, E. Masso, G. Panico, O. Pujolas, and F. Rompineve, *Phys. Rev. Lett.* **122**, 101301 (2019), [arXiv:1807.01707 \[hep-ph\]](#).
- [26] S. Ge, *Phys. Dark Univ.* **27**, 100440 (2020), [arXiv:1905.12182 \[hep-ph\]](#).

- [27] J. Liu, Z.-K. Guo, and R.-G. Cai, *Phys. Rev. D* **101**, 023513 (2020), [arXiv:1908.02662 \[astro-ph.CO\]](#).
- [28] G. B. Gelmini, J. Hyman, A. Simpson, and E. Vitagliano, *JCAP* **06**, 055 (2023), [arXiv:2303.14107 \[hep-ph\]](#).
- [29] N. Kitajima, J. Lee, K. Murai, F. Takahashi, and W. Yin, *Phys. Lett. B* **851**, 138586 (2024), [arXiv:2306.17146 \[hep-ph\]](#).
- [30] S. Ge, J. Guo, and J. Liu, *Phys. Rev. D* **109**, 123030 (2024), [arXiv:2309.01739 \[hep-ph\]](#).
- [31] Y. Gouttenoire and E. Vitagliano, *Phys. Rev. D* **110**, L061306 (2024), [arXiv:2306.17841 \[gr-qc\]](#).
- [32] Y. Gouttenoire and E. Vitagliano, *Phys. Rev. D* **109**, 123507 (2024), [arXiv:2311.07670 \[hep-ph\]](#).
- [33] R. Z. Ferreira, A. Notari, O. Pujolàs, and F. Rompineve, *JCAP* **06**, 020 (2024), [arXiv:2401.14331 \[astro-ph.CO\]](#).
- [34] D. I. Dunskey and M. Kongsore, *JHEP* **06**, 198 (2024), [arXiv:2402.03426 \[hep-ph\]](#).
- [35] Y. Gouttenoire, S. F. King, R. Roshan, X. Wang, G. White, and M. Yamazaki, (2025), [arXiv:2501.16414 \[hep-ph\]](#).
- [36] K. Sato, M. Sasaki, H. Kodama, and K.-i. Maeda, *Prog. Theor. Phys.* **65**, 1443 (1981).
- [37] H. Kodama, M. Sasaki, K. Sato, and K.-i. Maeda, *Prog. Theor. Phys.* **66**, 2052 (1981).
- [38] H. Kodama, M. Sasaki, and K. Sato, *Prog. Theor. Phys.* **68**, 1979 (1982).
- [39] K.-i. Maeda, K. Sato, M. Sasaki, and H. Kodama, *Phys. Lett. B* **108**, 98 (1982).
- [40] K. Jedamzik and J. C. Niemeyer, *Phys. Rev. D* **59**, 124014 (1999), [arXiv:astro-ph/9901293](#).
- [41] J. Liu, L. Bian, R.-G. Cai, Z.-K. Guo, and S.-J. Wang, *Phys. Rev. D* **105**, L021303 (2022), [arXiv:2106.05637 \[astro-ph.CO\]](#).
- [42] K. Hashino, S. Kanemura, and T. Takahashi, *Phys. Lett. B* **833**, 137261 (2022), [arXiv:2111.13099 \[hep-ph\]](#).
- [43] K. Hashino, S. Kanemura, T. Takahashi, and M. Tanaka, *Phys. Lett. B* **838**, 137688 (2023), [arXiv:2211.16225 \[hep-ph\]](#).
- [44] K. Kawana, T. Kim, and P. Lu, *Phys. Rev. D* **108**, 103531 (2023), [arXiv:2212.14037 \[astro-ph.CO\]](#).
- [45] M. Lewicki, P. Toczek, and V. Vaskonen, *JHEP* **09**, 092 (2023), [arXiv:2305.04924 \[astro-ph.CO\]](#).
- [46] Y. Gouttenoire and T. Volansky, *Phys. Rev. D* **110**, 043514 (2024), [arXiv:2305.04942 \[hep-ph\]](#).
- [47] M. M. Flores, A. Kusenko, and M. Sasaki, *Phys. Rev. D* **110**, 015005 (2024), [arXiv:2402.13341 \[hep-ph\]](#).
- [48] K. Hashino, S. Kanemura, T. Takahashi, M. Tanaka, and C.-M. Yoo, (2025), [arXiv:2501.11040 \[hep-ph\]](#).
- [49] C.-M. Yoo, T. Harada, and H. Okawa, *Phys. Rev. D* **102**, 043526 (2020), [Erratum: *Phys.Rev.D* 107, 049901 (2023)], [arXiv:2004.01042 \[gr-qc\]](#).
- [50] S. R. Coleman, V. Glaser, and A. Martin, *Commun. Math. Phys.* **58**, 211 (1978).
- [51] P. Mroz *et al.*, *Nature* **548**, 183 (2017), [arXiv:1707.07634 \[astro-ph.EP\]](#).
- [52] H. Niihura *et al.*, *Nature Astron.* **3**, 524 (2019), [arXiv:1701.02151 \[astro-ph.CO\]](#).
- [53] H. Niihura, M. Takada, S. Yokoyama, T. Sumi, and S. Masaki, *Phys. Rev. D* **99**, 083503 (2019), [arXiv:1901.07120 \[astro-ph.CO\]](#).
- [54] K. G. Arun *et al.* (LISA), *Living Rev. Rel.* **25**, 4 (2022), [arXiv:2205.01597 \[gr-qc\]](#).
- [55] K. Hashino, M. Kakizaki, S. Kanemura, P. Ko, and T. Matsui, *Phys. Lett. B* **766**, 49 (2017), [arXiv:1609.00297 \[hep-ph\]](#).
- [56] V. Vaskonen, *Phys. Rev. D* **95**, 123515 (2017), [arXiv:1611.02073 \[hep-ph\]](#).
- [57] A. Beniwal, M. Lewicki, J. D. Wells, M. White, and A. G. Williams, *JHEP* **08**, 108 (2017), [arXiv:1702.06124 \[hep-ph\]](#).
- [58] K. Hashino, R. Jinno, M. Kakizaki, S. Kanemura, T. Takahashi, and M. Takimoto, *Phys. Rev. D* **99**, 075011 (2019), [arXiv:1809.04994 \[hep-ph\]](#).
- [59] J. Ellis, M. Lewicki, and J. M. No, *JCAP* **04**, 003 (2019), [arXiv:1809.08242 \[hep-ph\]](#).
- [60] A. Alves, T. Ghosh, H.-K. Guo, K. Sinha, and D. Vagie, *JHEP* **04**, 052 (2019), [arXiv:1812.09333 \[hep-ph\]](#).
- [61] T. Alanne, T. Hugle, M. Platscher, and K. Schmitz, *JHEP* **03**, 004 (2020), [arXiv:1909.11356 \[hep-ph\]](#).
- [62] J. Ellis, M. Lewicki, M. Merchand, J. M. No, and M. Zych, *JHEP* **01**, 093 (2023), [arXiv:2210.16305 \[hep-ph\]](#).
- [63] M. J. Ramsey-Musolf, T. V. I. Tenkanen, and V. Q. Tran, (2024), [arXiv:2409.17554 \[hep-ph\]](#).
- [64] D. Bodeker and G. D. Moore, *JCAP* **05**, 009 (2009), [arXiv:0903.4099 \[hep-ph\]](#).
- [65] S. Sugiyama, M. Takada, and A. Kusenko, *Phys. Lett. B* **840**, 137891 (2023), [arXiv:2108.03063 \[hep-ph\]](#).
- [66] P. Tisserand *et al.* (EROS-2), *Astron. Astrophys.* **469**, 387 (2007), [arXiv:astro-ph/0607207](#).
- [67] P. Mróz *et al.*, *Nature* **632**, 749 (2024), [arXiv:2403.02386 \[astro-ph.GA\]](#).
- [68] P. Mróz *et al.*, *Astrophys. J. Lett.* **976**, L19 (2024), [arXiv:2410.06251 \[astro-ph.CO\]](#).
- [69] B. J. Kavanagh, “PBH bounds,” (2019).
- [70] C. L. Wainwright, *Comput. Phys. Commun.* **183**, 2006 (2012), [arXiv:1109.4189 \[hep-ph\]](#).
- [71] V. A. Kuzmin, V. A. Rubakov, and M. E. Shaposhnikov, *Phys. Lett. B* **155**, 36 (1985).
- [72] A. G. Cohen, D. B. Kaplan, and A. E. Nelson, *Ann. Rev. Nucl. Part. Sci.* **43**, 27 (1993), [arXiv:hep-ph/9302210](#).
- [73] S. Kanemura, M. Kikuchi, and K. Yagyu, *Nucl. Phys. B* **917**, 154 (2017), [arXiv:1608.01582 \[hep-ph\]](#).
- [74] S. R. Coleman and E. J. Weinberg, *Phys. Rev. D* **7**, 1888 (1973).
- [75] L. Dolan and R. Jackiw, *Phys. Rev. D* **9**, 3320 (1974).
- [76] A. Ashoorioon and T. Konstandin, *JHEP* **07**, 086 (2009), [arXiv:0904.0353 \[hep-ph\]](#).
- [77] C.-W. Chiang, Y.-T. Li, and E. Senaha, *Phys. Lett. B* **789**, 154 (2019), [arXiv:1808.01098 \[hep-ph\]](#).
- [78] P. Athron, C. Balazs, A. Fowlie, L. Morris, G. White, and Y. Zhang, *JHEP* **01**, 050 (2023), [arXiv:2208.01319 \[hep-ph\]](#).
- [79] R. R. Parwani, *Phys. Rev. D* **45**, 4695 (1992), [Erratum: *Phys.Rev.D* 48, 5965 (1993)], [arXiv:hep-ph/9204216](#).
- [80] G. Cynolter, E. Lendvai, and G. Pocsik, *Acta Phys. Polon. B* **36**, 827 (2005), [arXiv:hep-ph/0410102](#).
- [81] G. M. Pruna and T. Robens, *Phys. Rev. D* **88**, 115012 (2013), [arXiv:1303.1150 \[hep-ph\]](#).
- [82] C.-Y. Chen, S. Dawson, and I. M. Lewis, *Phys. Rev. D* **91**, 035015 (2015), [arXiv:1410.5488 \[hep-ph\]](#).